Magnetic Actuation of Surface Walkers: The Effects of Confinement and Inertia

Wen-Zhen Fang,[1,2] Seokgyun Ham,[2] Rui Qiao,[2,*] and Wen-Quan Tao[1]

[1] Key Laboratory of Thermo-Fluid Science and Engineering, MOE, Xi'an Jiaotong University, Xi'an, China

[2] Department of Mechanical Engineering, Virginia Tech, Blacksburg, Virginia, USA

Corresponding Email: ruiqiao@vt.edu

TOC Image

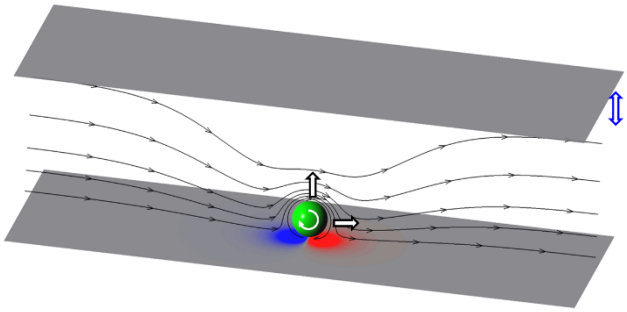

Abstract

Driven by a magnetic field, the rotation of a particle near a wall can be rectified into a net translation. The particles thus actuated, or surface walkers, are a kind of active colloids that find application in biology and microfluidics. Here, we investigate the motion of spherical surface walkers confined between two walls using simulations based on the immersed-boundary lattice Boltzmann method. The degree of confinement and the nature of the confining walls (slip vs. no-slip) significantly affect a particle's translation speed and can even reverse its translation direction. When the rotational Reynolds number Re_ω is larger than 1, inertia effects reduce the critical frequency of the magnetic field, beyond which the sphere can no longer follow the external rotating field. The reduction of the critical frequency is especially pronounced when the sphere is confined nearly a no-slip wall. As Re_ω increases beyond 1, even when the sphere can still rotate in the synchronous regime, its translational Reynolds number Re_T no longer increases linearly with Re_ω and even decrease when Re_ω exceeds ~10.

Introduction

The manipulation of microscopic particles in a liquid environment is crucial in many applications.[1-4] Methods leveraging electrical, acoustic, and magnetic forces have been developed, e.g., dielectrophoresis, acoustophoresis, and magnetophoresis. Methods based on magnetic forces are often desirable because of their safety and the ability of magnetic fields to penetrate most media without adverse effects.[5-9] Among the magnetism-based methods, the surface walker mechanism has attracted much attention. By applying a rotating or alternating magnetic field, one drives the rotation of magnetic particles even if the field is weak (e.g., ~ a few mT). For a particle in unbounded, quiescent liquids, its rotation does not lead to net translation due to symmetry. However, if a particle is located near a surface, the symmetry is broken, and its rotation can be rectified into net translation.[10-12] Particles thus actuated are called surface walkers and can be used to induce flow,[13] deliver cargos at microscale,[14-15] and manipulate cells[16]. A variety of surface walkers have been demonstrated, e.g., DNA-linked doublets made of paramagnetic colloidal particles and colloidal chains.[13, 17] Many intriguing phenomena have been reported (see Ref. 4 for a recent review). For example, in a suspension of magnetic particles rotating above a solid wall, particle clusters can emerge from fingering instability;[12, 18]; near a wall, a chain of spinning particles moves faster than individual particles;[19] the hydrodynamic bound state of a pair of particles is frequency-dependent,[20] and a cloud of particles can exhibit "flocking" behavior when energized by a vertical alternating magnetic field.[21]

Fundamentally, the dynamics of surface walkers depends on the nature of the confining boundaries (slip or no-slip), the degree of confinement (e.g., the distance of a particle to the nearby wall and the presence of multiple confining boundaries), and the frequency of the magnetic field (e.g., beyond a certain critical frequency, the surface walker's translation speed can decrease dramatically).[22] Understanding these dependencies by experiments alone is difficult, and numerical and theoretical modeling can be helpful.

In theoretical modeling, the motion of a particle near an extended no-slip wall can be described as a linear combination of the fundamental solutions to the Stokes equations: a stokeslet singularity, a source singularity, a stokeslet singularity, and a rotlet singularity.[23-25] Spagnolie and Lauga compared the motion

of a sphere near a single wall predicted based on the far-field approximation and from full solutions of the Stokes equation in details.[26] They showed that the far-field approximation is accurate if a sphere's distance to the wall is larger than its diameter, but cannot accurately account for the near-field effects when the sphere gets even closer to the wall. These studies provided critical insights into the actuation of surface walkers, but their extension to more complicated situations (e.g., if there are multiple confining boundaries or the inertia effects are not negligible) is challenging.

In numerical modeling, the dynamics of surface walkers can be studied using Stokesian dynamics, force-coupling method and direct numerical simulations. In Stokesian dynamics, the particle-wall/particle hydrodynamic interactions are considered using a resistance/mobility tensor.[13, 27-29] This method can be readily applied only in semi-infinite[13] or infinite domains.[29] The force-coupling method represents particles by locally distributed body forces to the Navier-Stokes (NS) equations (or Stokes equations) to account for fluid-particle hydrodynamic interactions. It has been used to study the collective dynamics of rotating particles.[30-31] In direct numerical simulations, the two-way hydrodynamic coupling between the fluid and particles is resolved using various methods (e.g., the finite element method[32-33] or the lattice Boltzmann method (LBM).[34-35] To date, the above methods have been used to simulate particle dynamics in the absence of inertia effects. However, for magnetic surface walkers, their rotational Reynolds number can be larger than 1. Hence, inertia effects can come into play, and the full NS equations must be solved.[36-37] Research in this regime is limited. For example, Zeng *et al*.[38] investigated the effect of a single wall on a translating sphere, and Liu *et al*.[39] investigated the wall effect on a center-fixed rotating sphere at finite rotational Reynolds number. These studies focused on calculating the wall-induced lift/drag forces and did not directly address the translation and rotation of particles actuated by external fields.

In this work, we study the dynamics of surface walkers (spherical ferromagnetic particles) actuated by a rotating magnetic field. We solve the fluid flow in the low but non-zero Reynolds number regime using LBM and handle the fluid-particle interactions using the immersed boundary method (IBM).[40-41] We first examine how confinement affects the critical frequency of the magnetic field. Next, we systematically

examine how the nature of confining boundaries and the degree of confinements affect the translation of the surface walker for rotational Reynolds numbers ranging from 0.01 to ~10.

Materials and Methods

Simulation system and mathematical models

We study the actuation of a single ferromagnetic sphere (radius: r) positioned at a distance h from a solid wall (see Fig. 1). An upper boundary is located at L_z above the lower wall, and the space between the lower wall and the upper boundary is filled with liquids. The system is periodic in the directions parallel to the wall (x- and y-directions).

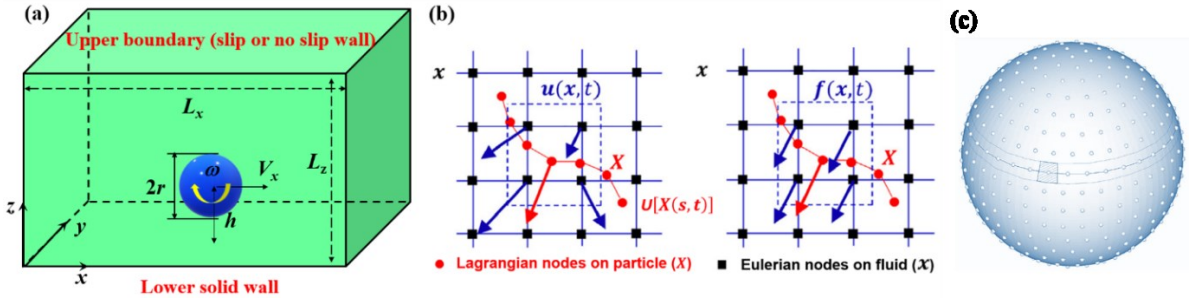

Figure 1. *Simulation system and the immersed boundary method.* (**a**) Actuation of a spherical magnetic particle by a rotating magnetic field. (**b**) A schematic of the velocity interpolation and force spreading between the Lagrangian nodes and the Eulerian nodes in the immersed boundary method. (**c**) Distribution of the Lagrangian nodes (empty circles) on a spherical solid particle.

The fluid motion is governed by the NS equations:

$$\frac{\partial \rho}{\partial t} + \nabla \cdot (\rho \boldsymbol{u}) = 0 \tag{1}$$

$$\frac{\partial \rho \boldsymbol{u}}{\partial t} + \nabla \cdot (\rho \boldsymbol{u}\boldsymbol{u}) = -\nabla p + \nabla \left[\mu \left(\nabla \boldsymbol{u} + (\nabla \boldsymbol{u})^T \right) \right] + \boldsymbol{F} \tag{2}$$

where ρ is the density; $\boldsymbol{u}$ is the fluid velocity; p is the pressure; μ is the dynamic viscosity; and $\boldsymbol{F}$ is the sum of the fluid body force and the hydrodynamic forces exerted by the particle. The no-slip boundary condition is imposed on the lower solid wall and the particle's surface. On the upper boundary, either the no-slip boundary condition or the zero-shear stress boundary condition is imposed, which mimics a solid wall or a free fluid surface, respectively.

The translation of the particle is governed by

$$m_p \frac{d\boldsymbol{U}_p}{dt} = -\int_s \boldsymbol{\sigma} \cdot d\boldsymbol{s} + F_e \tag{3}$$

where $\boldsymbol{U}_p$ is the particle's translational velocity; m_p is the particle mass; $\boldsymbol{\sigma}$ is the fluid stress tensor; $\boldsymbol{s}$ denotes the particle surface, and F_e denotes the external body force. The rotation of the particle is governed by [42-43]

$$I_p \frac{d\boldsymbol{\omega}}{dt} = -\int_s \left(\boldsymbol{X}_s - \boldsymbol{X}_o\right) \times \left(\boldsymbol{\sigma} \cdot d\boldsymbol{s}\right) + \boldsymbol{m} \times \boldsymbol{B} \tag{4}$$

where $\boldsymbol{\omega}$ is the angular velocity of the particle; I_p is the particle's moment of inertial ($I_p = 0.4\, m_p r^2$ since the particle is spherical here); $\boldsymbol{X}_s$ and $\boldsymbol{X}_o$ denote the position on the particle surface and the center of the particle; m is the magnetic moment. Here a rotating magnetic field is applied, and it is given by $\boldsymbol{B} = B\cos(2\pi f_B t)\, \boldsymbol{i} - B\sin(2\pi f_B t)\, \boldsymbol{j}$, where B and f_B are the strength and rotating frequency of the magnetic field, respectively.

Numerical methods and implementation

The above governing equations are solved using LBM (see Eqs. 5-10 below) and IBM (see Eqs. 12-16 below). LBM is adopted as an efficient numerical tool to solve the NS equations (Eq. 1 and Eq. 2), and IBM is used to deal with the hydrodynamic interactions between the fluid and sphere. The basic idea of IBM is to use the force density $\boldsymbol{F}(x, t)$ in the NS equations to mimic a boundary (e.g., no-slip) that affects the fluid. The immersed boundary-lattice Boltzmann method (IB-LBM) allows for a two-way coupling between the dynamics of particles and the fluids. The IB-LBM method uses a set of Lagrangian nodes $\boldsymbol{X}(s)$ (physical quantities on Lagrangian nodes are denoted with Capital letters) and a set of Eulerian nodes $\boldsymbol{x}$ (physical quantities on Eulerian nodes are denoted with Lowercase letters) simultaneously. The former is an ensemble of maker nodes on the surface of particles, which can move in the space; the latter consists of fixed lattice nodes for solving the fluid flow. The velocity of the Lagrangian nodes is interpolated from the Eulerian nodes to enforce the no-slip condition on the particle surface. Meanwhile, the force density calculated on the Lagrangian nodes should be spread to Eulerian nodes such that the fluid acts as if there is a boundary. The velocity interpolation and force spreading between the two node systems are illustrated in Fig. 1b.

Instead of solving the NS equations directly, LBM solves the evolution equation of the density distribution function (see Eq. 5 below) which can recover to the NS equations by Chapmen-Enskog expansion. In this work, three-dimensional nineteen-velocity (D3Q19) multi-relation-time (MRT) LBM is adopted to solve the evolution equation [44-45]

$$g_\alpha\left(\boldsymbol{x}+\boldsymbol{e}_\alpha\delta t,t+\delta t\right)-g_\alpha\left(\boldsymbol{x},t\right)=-\left(\mathbf{M}^{-1}\Lambda\mathbf{M}\right)_{\alpha\beta}\left[g_\beta-g_\beta^{eq}\right]+\delta tF_\alpha^{'} \tag{5}$$

where $g(\boldsymbol{x}, t)$ is the density distribution function at the lattice site $\boldsymbol{x}$ (Eulerian nodes) and time t and g^{eq} is the equilibrium distribution function; and $\boldsymbol{e}_\alpha$ is the discrete velocity along the α direction, defined as

$$\boldsymbol{e}_\alpha=\begin{bmatrix}0,\ 1,-1,\ 0,\ 0,\ 0,\ 0,1,-1,1,-1,1,-1,1,-1,0,0,0,0\\ 0,\ 0,\ 0,\ 1,-1,\ 0,\ 0,1,1,-1,-1,0,0,0,0,1,-1,1,-1\\ 0,\ 0,\ 0,\ 0,\ 0,\ 1,-1,0,0,0,0,1,1,-1,-1,1,1,-1,-1\end{bmatrix} \tag{6}$$

Using an orthogonal transformation matrix **M**, the right side of Eq. 5 can be mapped into the moment space and rewritten as[44-45]

$$\boldsymbol{m}'^{*}=\boldsymbol{m}'-\Lambda\left(\boldsymbol{m}'-\boldsymbol{m}'^{,eq}\right)+\delta_t\left(\mathbf{I}-\frac{\Lambda}{2}\right)\boldsymbol{S} \tag{7}$$

where $\boldsymbol{m}'=\mathbf{M}\boldsymbol{g}$ and $\boldsymbol{m}'^{,eq}=\mathbf{M}\boldsymbol{g}^{eq}$. $\boldsymbol{\Lambda}$ is the diagonal collision matrix given by

$$\Lambda=\mathrm{diag}(\tau_0^{-1},\tau_e^{-1},\tau_\varepsilon^{-1},\tau_0^{-1},\tau_q^{-1},\tau_0^{-1},\tau_q^{-1},\tau_0^{-1},\tau_q^{-1},\tau_v^{-1},\tau_\pi^{-1},\tau_v^{-1},\tau_\pi^{-1},\tau_v^{-1},\tau_v^{-1},\tau_v^{-1},\tau_t^{-1},\tau_t^{-1},\tau_t^{-1}) \tag{8}$$

By definition, the equilibrium $\boldsymbol{m}'^{,eq}$ has the expression

$$\boldsymbol{m}'^{,eq}=\rho\begin{pmatrix}1,\ -11+19(u_x^2+u_y^2+u_z^2),3-\frac{11}{2}(u_x^2+u_y^2+u_z^2),\\ u_x,-\frac{2}{3}u_x,u_y,-\frac{2}{3}u_y,u_z,-\frac{2}{3}u_z,\frac{1}{2}(2u_x^2-u_y^2-u_z^2),\\ u_y^2-u_z^2,\frac{1}{2}(u_y^2-u_z^2),u_xu_y,u_xu_z,0,0,0\end{pmatrix}^T \tag{9}$$

In Eq. 7, $\boldsymbol{S}$ is the forcing term in the moment space with $\left(\mathbf{I}-\frac{\Lambda}{2}\right)\boldsymbol{S}=\mathbf{M}\boldsymbol{F}'$, and is given as[44]

$$\boldsymbol{S}=\begin{pmatrix} 0,38(u_xF_x+u_yF_y+u_zF_z),-11(u_xF_x+u_yF_y+u_zF_z),F_x, \\ -2/3F_x,F_y,-2/3F_y,F_z,-2/3F_z,2(2u_xF_x-u_yF_y-u_zF_z), \\ -2u_xF_x+u_yF_y+u_zF_z,2(u_yF_y-u_zF_z),-u_yF_y+u_zF_z, \\ u_xF_y+u_yF_x,u_yF_z+u_zF_y,u_xF_z+u_zF_x,0,0,0 \end{pmatrix}^T \tag{10}$$

where the total force density is given by

$$\boldsymbol{F}=\boldsymbol{F}_e+\boldsymbol{f}_s \tag{11}$$

where $\boldsymbol{F}_e$ is the external force density, such as the gravity; $\boldsymbol{f}_s$ is the hydrodynamic force on the Eulerian node calculated by the IBM[46]

$$\boldsymbol{f}_s=\int_\Gamma \boldsymbol{F}_s\left[\boldsymbol{X}(s,t)\right]\delta_h\left(\boldsymbol{x}-\boldsymbol{X}(s)\right)ds=\sum_s F_s\left[\boldsymbol{X}(s,t)\right]\delta_h\left(\boldsymbol{x}-\boldsymbol{X}(s)\right)\delta_s \tag{12}$$

where Γ represents the immersed boundary of the particle; $\boldsymbol{F}_s$ is the hydrodynamic force on the boundary point $\boldsymbol{X}(s)$ (Lagrangian node); δ_h is the smooth approximation of the Dirac's delta function

$$\delta_h(\boldsymbol{x})=\frac{1}{\Delta_x\Delta_y\Delta_z}\delta_h\left(\frac{x}{\Delta_x}\right)\delta_h\left(\frac{y}{\Delta_y}\right)\delta_h\left(\frac{z}{\Delta_z}\right) \tag{13}$$

with

$$\delta_h(d)=\begin{cases}\left(3-2|d|+\sqrt{1+4|d|-4|d|^2}\right)/8, & |d|<1\\ \left(5-2|d|+\sqrt{-7+12|d|-4|d|^2}\right)/8, & 1\le|d|\le 2\\ 0, & |d|>2\end{cases} \tag{14}$$

In this work, the direct-forcing method is adopted to calculate the hydrodynamic force between the fluid and particle [46]

$$\boldsymbol{F}_s\left[\boldsymbol{X}(s,t)\right]=2\rho\frac{\boldsymbol{U}^{\mathrm{d}}-\boldsymbol{U}^{\mathrm{noF}}}{\delta t} \tag{15}$$

where $\boldsymbol{U}^{\mathrm{d}}$ and $\boldsymbol{U}^{\mathrm{noF}}$ are the desired velocity and unforced velocity at forcing boundary points, respectively. $\boldsymbol{U}^{\mathrm{noF}}$ can be calculated by

$$\boldsymbol{U}^{noF}\left[\boldsymbol{X}(s,t)\right]=\int_{\boldsymbol{x}}\boldsymbol{u}^{noF}\delta_h\left(\boldsymbol{x}-\boldsymbol{X}(s)\right)dx \tag{16}$$

where $\boldsymbol{u}^{noF}$ is the unforced velocity on the Eulerian nodes, which is obtained using

$$\boldsymbol{u}^{noF}=\frac{1}{\rho}\sum_{\alpha}\boldsymbol{e}_{\alpha}g_{\alpha} \tag{17}$$

The fluid density and physical velocity on Eulerian nodes are obtained by the summation of and the moment of the density distribution function:

$$\rho=\sum_{\alpha}g_{\alpha} \tag{18}$$

$$\boldsymbol{u}=\frac{1}{\rho}(\sum_{\alpha}\boldsymbol{e}_{\alpha}g_{\alpha}+\boldsymbol{f}_s) \tag{19}$$

The above fluid-particle momentum force $\boldsymbol{F}_s$ and hydrodynamic torques lead to the motion of particle, which is governed by Newton's law (Eq. 3-4).The hydrodynamic force term (first term on the right side of Eq. 3) is calculated by[42-43]

$$-\int_S\boldsymbol{\sigma}\cdot d\boldsymbol{s}=-\int_V\boldsymbol{F}_s dV+m_f\frac{d\boldsymbol{U}_p}{dt} \tag{20}$$

where $m_f=\rho V$, and V is the volume of the particle. The hydrodynamic torque term (the first term on the right side of Eq. 4) is calculated by

$$-\int_s\left(\boldsymbol{X}_s-\boldsymbol{X}_o\right)\times\left(\boldsymbol{\sigma}\cdot d\boldsymbol{s}\right)=-\int_V\left(\boldsymbol{X}_s-\boldsymbol{X}_o\right)\times\boldsymbol{F}_s dV+I_f\frac{d\boldsymbol{\omega}_p}{dt} \tag{21}$$

where I_f is the inertial moment of fluid occupied by the particle. Thus, Eq. 3 and Eq. 4 are discretized as

$$\boldsymbol{U}_p^{n+1}=\boldsymbol{U}_p^n+\frac{1}{m_p}\left(-\sum_S\boldsymbol{F}_s^n\Delta\boldsymbol{s}\delta x+\boldsymbol{F}_e\right)\delta t+\left(m_f/m_p\right)\left(\boldsymbol{U}_p^n-\boldsymbol{U}_p^{n-1}\right) \tag{22}$$

$$\boldsymbol{\omega}^{n+1}=\boldsymbol{\omega}^n+\frac{1}{I_p}\left(-\sum_s\left(\boldsymbol{X}_s-\boldsymbol{X}_c\right)\times\boldsymbol{F}_s\Delta\boldsymbol{s}\delta x+\boldsymbol{F}_e\right)\delta t+\left(I_f/I_p\right)\left(\boldsymbol{\omega}^n-\boldsymbol{\omega}^{n-1}\right) \tag{23}$$

The particle's position is updated by the translational velocity at time n and n+1

$$\boldsymbol{X}_p^{n+1} = \boldsymbol{X}_o^n + 0.5\left(\boldsymbol{U}_p^{n+1} + \boldsymbol{U}_p^n\right) \tag{24}$$

And the desired velocity at each Lagrangian node is updated by

$$\boldsymbol{U}_d^{n+1} = \boldsymbol{U}_p^{n+1} + \boldsymbol{\omega}^{n+1} \times \left(\boldsymbol{X}_s - \boldsymbol{X}_o\right) \tag{25}$$

Here, a uniform lattice spacing is used for the Eulerian nodes, with each grid step representing $r/6$. For a typical value of $r = 12$ μm in this work, $\delta x = 2$ μm and the corresponding time step is $\delta t = 1$ μs. In most of cases, the simulation domain is chosen to be $60r \times 30r \times 30r$ with a grid number ~12,000,000 (see Table 1 for a grid dependence test). To implement the no-slip and slip upper boundary conditions, the half-way bounce back scheme and specular reflection scheme are adopted, respectively.[47] The spherical particle's surface is discretized into 574 Lagrangian nodes (see Fig. 1c) using the method in Ref. 43. The spacing between two neighboring Lagrangian nodes is approximately equal to the spacing between the Eulerian nodes. Grid studies show that these node spacings are sufficient to obtain an accurate prediction of the particle dynamics.

Numerical tests

We validate our code in three sets of tests relevant to the actuation of surface walkers using rotating magnetic fields: the rotation of a sphere in a rotating magnetic field, the rotation of a sphere near a planar wall, and the translation of a sphere near a planar wall.

First, we simulate the rotation of a sphere ($r = 48$ μm; $M = 80\pi$ A/m) in a periodic box filled with a fluid ($\mu = 10^{-3}$ Pa·s). The box measures $40r \times 40r \times 40r$, which is large enough to mimic an unbound fluid. The strength of the magnetic field is $B = 3$mT. The rotation of a magnetic sphere in a field rotating at a frequency of f_B exhibits two regimes. When f_B is below the critical frequency f_c, we have the synchronous regime, in which the sphere's rotational frequency (f) is equal to f_B. When $f_B > f_c$, we have the asynchronous regime, in which the sphere rotates with a mean frequency lower than f_B. For ferromagnetic magnetic spheres in an unbounded fluid, in the limit of small Re_ω, f_c is given by [48-49]

$$f_c = mB/2\pi\gamma = MB/(12\pi\mu) \quad (26)$$

where m=4πMr^3/3 is the particle's magnetic moment (M: sphere's magnetization), B is the strength of the magnetic field, and γ =8πμr^3 is the rotational drag coefficient of a sphere in an unbound fluid. For $f_B > f_c$, the rotational frequency of the sphere follows

$$f = f_B\left[1 - \sqrt{1 - (f_c/f_B)^2}\right] \quad (27)$$

With the parameters chosen, Eq. 26 predicts a critical frequency of f_c = 20 Hz. Figure 2a shows the variation of the sphere's mean rotational frequency f with f_B. The computed critical frequency f_c and the evolution of f at $f_B > f_c$ both agree well with those predicted by Eq. 26 and 27.

Next, we simulate the rotation of a sphere near a solid wall. The sphere is fixed at a height h above the wall and rotates in the clockwise direction with angular speed ω. The hydrodynamic force F_h experienced by the sphere can be given as

$$F_h = \pi\mu r^2 \omega f_x(h/r, Re_\omega) \quad (28)$$

where Re_ω is the rotational Reynolds number given by

$$Re_\omega = \rho\omega r^2/\mu \quad (29)$$

In the limit of small Re_ω and r/h, f_x is given by[39, 50]

$$f_x(h/r) = \frac{3}{4}\left(\frac{r}{h}\right)^4\left(1 - \frac{3}{8}\frac{r}{h}\right) \quad (30)$$

We set h = 1.5r and vary the system size (see Fig. 1a) systematically to examine how large the system must be for f_x to converge to the prediction by Eq. 30. Re_ω is set to 0.07 in the simulation. Table 1 summarizes the computed f_x and the prediction by Eq. 30. We observe that the hydrodynamic force is more sensitive to the domain size in the x-direction than in the y- and z-directions. With L_x = 60r, L_y = 30r, and L_z=30r, there are ~12,000,000 lattice points in the computational domain and the computed hydrodynamic force is ~5% higher than the analytical solution. Therefore, as a compromise between accuracy and computational cost, this domain size is used in the rest of this work.

Table 1. Effect of domain size on the hydrodynamic force

domain size			f_x
L_x/r	L_y/r	L_z/r	
30	30	30	0.1276
30	30	40	0.1278
30	40	30	0.1272
40	30	30	0.121
60	30	30	0.117
∞	∞	∞	0.111[39, 50]

Finally, we simulate the translation of a sphere near a wall without rotation. The center of the sphere is fixed at various height h above the wall, and a constant force F_d is applied to the sphere in the x-direction. For a sphere moving parallel to a wall at a speed V_x, it experiences a drag force given by

$$F_d = 6\pi\mu r V_x f_u(h/r, \mathrm{Re_T}) \tag{31}$$

where $\mathrm{Re_T} = 2\rho V_x r/\mu$ is the translational Reynolds number. In the limit of small $\mathrm{Re_T}$ and small r/h, Faxen obtained f_u using the method of reflections[50]

$$f_u(h/r) = 1 - \frac{9}{16}\left(\frac{r}{h}\right) + \frac{1}{8}\left(\frac{r}{h}\right)^3 - \frac{45}{256}\left(\frac{r}{h}\right)^4 - \frac{1}{16}\left(\frac{r}{h}\right)^5 \tag{32}$$

We simulate the sphere movement at $Re_T = 5\times10^{-4}$ using the system shown in Fig. 1a. We set $L_x = 60r$, $L_y = 30r$, and $L_z = 30r$ so that the sphere is effectively in a semi-infinite liquid. Figure 2b compares the f_u obtained in our simulations with Eq. 32, and a very good agreement with Eq. 32 is obtained.

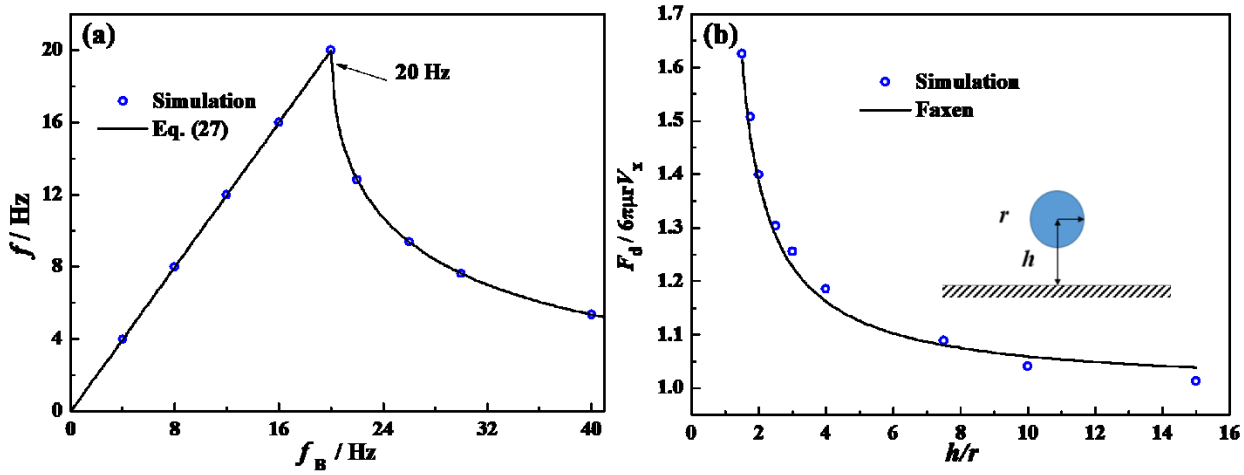

Figure 2. (**a**) The mean rotational frequency of a sphere actuated by a rotating magnetic field. The sphere (r = 48 μm; M = 80π A/m) is immersed in bulk. (**b**) The hydrodynamic force experienced by a sphere translating parallel to a no-slip wall without rotation.

Results and Discussion

We study how confinement and inertia affect the motion of spheres actuated by a rotating magnetic field. A sphere rotating at a distance from a wall experiences a host of forces in the vertical direction, e.g., gravity, buoyancy, *etc.,* which may drive it toward a new height, leading to a change of its confinement and complicating the study of how confinement affects its motion. Therefore, in first two subsections, we assume that this lift force is balanced by external forces. We thus fix the sphere's height but allow it to rotate and translate laterally. In the final subsection, we remove this assumption and study the motion of a sphere released from an initial height under the actuation of a magnetic field. The data from this study show that the results in first two subsections are also applicable to situations in which a sphere rises/settles slowly near a wall.

Confinement effects

Here we study how the degree of confinement and the nature of the confining surface affect the translation of a magnetically actuated sphere. The sphere has a radius of 12 μm and a magnetization of M=2×10^{4}A/m. The frequency of the rotating field is 20 Hz; the sphere rotates in the clockwise direction synchronously with the field. Re_ω is 0.018, and thus inertia effects are negligible. Without losing generality, we fix the sphere at h = 1.5r above the lower no-slip wall. The upper boundary, located at L_z above the lower wall, is either a no-slip wall or a slip wall (see Fig. 1a). The degree of confinement, as characterized by $k = r/L_z$, is varied between 1/30 and 1/3.

The sphere's velocity computed in these simulations is shown in Fig. 3a. We first examine the sphere's movement when the upper confining wall has a no-slip surface. At r/L_z = 1/30, the sphere moves in the positive x-direction; as r/L_z increases, the sphere's velocity decreases, and even becomes negative (e.g., at r/L_z = 1/4). At r/L_z = 1/3, when the sphere is positioned precisely halfway between the two walls, its velocity is zero. To understand these results, we performed additional simulations in which the rotating sphere's center is fixed but other conditions are unchanged. Measuring the horizontal hydrodynamic force

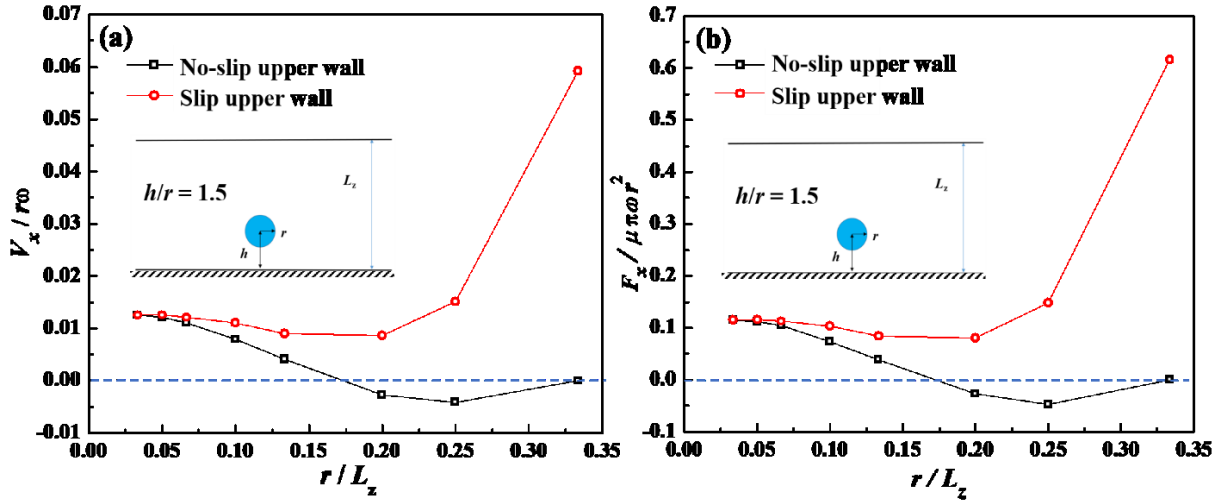

Figure 3. (a) The effect of confinement on the translation velocity of a magnetically actuated sphere. (**b**). The hydrodynamic force acting on a rotating sphere whose center is fixed between two walls. In both panels, the sphere is positioned at $h = 1.5r$ and rotates clockwise. The lower wall has a no-slip surface.

F_x experienced by these spheres helps understand how free rotating spheres moves, e.g., if F_x on a center-fixed sphere is positive, then the sphere will have a positive velocity if it is set free. Figure 3b shows that the variation of F_x on a center-fixed sphere as a function of r/L_z closely follows the trend of the velocity V_x shown in Fig. 3a, e.g., at $r/L_z = 1/4$, F_x is negative, consistent with the negative V_x seen in Fig. 3a. Therefore, below we focus on understanding the evolution of F_x (in particular its sign reversal) as r/L_z changes.

At $r/L_z = 1/30$, a center-fixed sphere rotating clockwise above a no-slip wall experiences a positive F_x. F_x can be decomposed into four components (see Fig. 4a): the horizontal component of the viscous forces on the sphere's top and bottom half ($F_{x,v}^T$, and $F_{x,v}^B$) and the horizontal component of the pressure force on the sphere's top and bottom half ($F_{x,p}^T$ and $F_{x,p}^B$). $F_{x,v}^B$ is positive and $F_{x,v}^T$ is negative, which are consistent with the flow field induced by the sphere (see Fig. 5a). Note that the viscous force $\boldsymbol{F}_v^\Gamma$ and the pressure force $\boldsymbol{F}_p^\Gamma$ on a piece of surface (Γ) of the sphere are defined as

$$\begin{cases} \boldsymbol{F}_v^\Gamma = \int_\Gamma \boldsymbol{\tau} \cdot d\boldsymbol{s} \\ \boldsymbol{F}_v^\Gamma = \int_\Gamma -p\boldsymbol{I} \cdot d\boldsymbol{s} \end{cases} \tag{33}$$

where $\boldsymbol{\tau}$ is the viscous stress tensor and $\boldsymbol{I}$ is the identity tensor. When a sphere rotates clockwise near the no-slip, lower wall, the flow field features a strong circulating flow surrounding the sphere and a weak, more global flow in the positive x-direction that extends quite far from the sphere. The circulating flow

imparts a positive $F_{x,v}^{B}$ and a negative $F_{x,v}^{T}$ on the sphere. These forces cancel each other to a large extent. However, because of the proximity of the no-slip wall to the sphere's bottom surface and hence larger velocity gradient on the sphere's bottom surface than on its top surface, the net viscous force on the sphere is positive (see Fig. 4a).

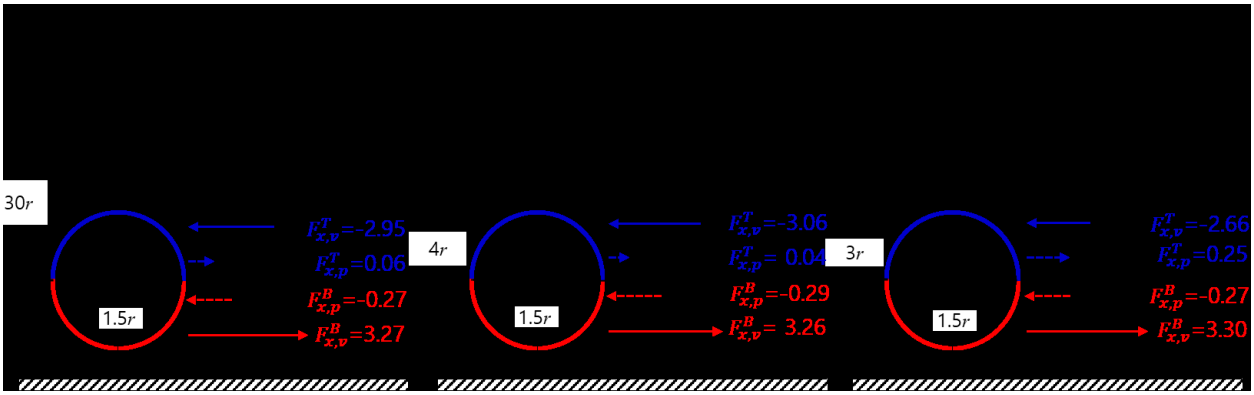

Figure 4. The horizontal hydrodynamic forces experienced by a center-fixed sphere confined between two walls. (**a**) r/L_z = 1/30 and upper boundary is a no-slip wall. (**b**) r/L_z = 1/4 and upper boundary is a no-slip wall. (**c**) r/L_z = 1/3 and upper boundary is a slip wall. The horizontal force F_x is divided into $F_{x,v}^{T}$, $F_{x,p}^{T}$, $F_{x,v}^{B}$ and $F_{x,p}^{B}$ (subscript p (v) denotes the pressure (viscous) components; superscript T (B) corresponds to the top (bottom) surface). The arrows denote the direction and magnitude of the forces (the magnitude is not to the scale because of the large difference between the viscous and pressure forces). All forces are normalized by $\pi\mu r^2\omega$.

As shown in Fig. 5a and also reported in previous studies,[39] the circulating flow increases the fluid pressure near the bottom front side of the sphere (red region in Fig. 5a) but reduces that near its bottom back side (blue region in Fig. 5a). This pressure imbalance leads to a negative $F_{x,p}^{B}$ on the sphere's bottom half. Meanwhile, the weak global flow in the positive direction imparts a positive pressure force $F_{x,p}^{T}$ on the sphere's top half. Since the circulating flow is stronger than the weak global flow, the net pressure force is negative (see Fig. 4a). The net pressure force is weaker than the viscous force, thus resulting in a positive F_x. Inspection of the force shown in Fig. 4a shows that F_x is more than 30 times weaker than $F_{x,v}^{B}$. The key point is that the significant viscous force on a sphere's top half and the net negative pressure force on the sphere cancel horizontal viscous force on its bottom half, leading to a weak driving force sphere translation.

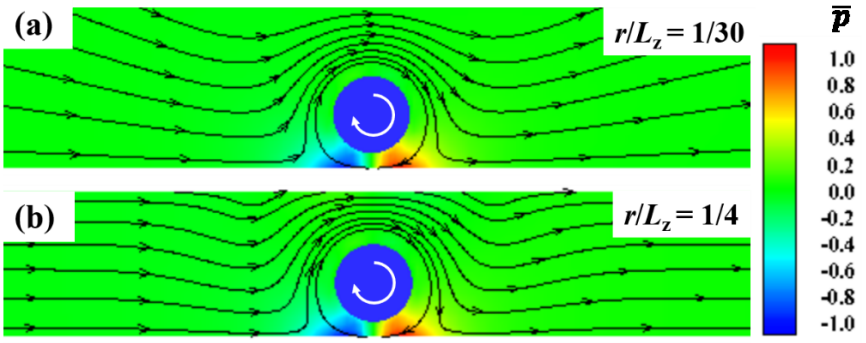

Figure 5. The flow and pressure fields near a rotating sphere between two no-slip walls separated by $L_z = 30r$ (**a**) and $L_z = 4r$ (**b**). The sphere is fixed at a height of $h/r = 1.5$ above the lower wall. The pressure is normalized by $\mu\omega$ and is color-coded ($\bar{p} = (p - p_{ref})/\mu\omega$).

As r/L_z increases, the F_x experienced by a center-fixed rotating sphere decreases. At $r/L_z = 1/4$, F_x becomes negative. The reversal of F_x is a result of the modified interplay between the viscous and pressure forces at the enhanced confinement. Because the circulating flow near the sphere's bottom half is little affected by the enhanced confinement by the upper wall, the velocity gradient and pressure field near the bottom half of the sphere do not differ much from those at $r/L_z = 1/30$ (cf. Fig. 5a and 5b). Therefore, $F_{x,v}^B$ and $F_{x,p}^B$ remains similar to that for $r/L_z = 1/30$ (see Fig. 4b). However, $F_{x,v}^T$ on the sphere's top half, becomes considerably more negative because the velocity gradient on the sphere's top surface increases with the enhanced confinement. As shown in Fig. 4b, the increased $F_{x,v}^T$ cancels the positive $F_{x,v}^B$ more greatly than that at $r/L_z = 1/30$. Meanwhile, the positive $F_{x,p}^T$ on the sphere's top half is weakened so that the total horizontal pressure force now overwhelms the horizontal viscous force, which leads to the reversal of F_x. Overall, the key point is that the force (velocity) reversal is due to the inherent cancelation of $F_{x,v}^B$ by $F_{x,v}^T$ for rotating surface walkers and the enhancement of this cancellation as confinement is increased.

As r/L_z increases toward 1/3, at which the sphere is positioned in the middle of the upper and lower no slip walls, F_x approaches zero as expected due to symmetry.

Finally, we examine the sphere's movement when the upper confining boundary is a slip wall. When r/L_z is small, the flow near the sphere is hardly affected by the upper wall, e.g., at $r/L_z = 1/30$, the gradient of the fluid velocity near the sphere's north pole is nearly unchanged when the upper boundary is

switched from a no-slip to slip wall (see Fig. S1 in the Supporting Information). Therefore, the translation of the sphere is similar, regardless of the nature of the upper boundary. However, as the slip wall moves closer to the sphere, the circulating flow near a rotating sphere's top surface is impeded much less than when the upper boundary is a no-slip wall. Therefore, the negative $F_{x,v}^{T}$ on the sphere's top surface is weaker and the net horizontal viscous force decreases less compared to the situation when the upper boundary has a no-slip wall. This explains why the decrease of a sphere's translation velocity is milder than when the upper boundary is a no-slip wall (see Fig. 3a).

At $r/L_z = 1/3$, when the sphere is exactly halfway between the two walls, the gradient of the velocity near the sphere's top surface is much smaller than that near the sphere's bottom surface (see Fig. S1 in the Supporting Information). Therefore, the positive $F_{x,v}^{B}$ on the sphere's bottom half is not much canceled by the negative $F_{x,v}^{T}$ (see Fig. 4c). Due to symmetry, the positive pressure force on the sphere's top and the negative pressure force on the sphere's bottom almost canceled out each other. This leads to a large positive net force on the sphere, and thus a large translation velocity (see Fig. 3b and Fig. 3a).

Inertia effects

Below we investigate the effect of inertia on the rotation and translation of spheres confined above a solid wall. The upper boundary is positioned at $L_z = 30r$ so that the sphere is essentially in a semi-infinite fluid. The sphere is fixed at the height of $1.5r$ above the lower wall in all simulations (see Fig. 1a). The strength of the magnetic field is the same as that used in Fig. 2a.

We first examine the rotation of wall-confined spheres in a rotating magnetic field for $\mathrm{Re}_\omega \lesssim 1$. Figure 6a shows that, compared to that in the unbounded fluids, f_c is reduced to 18 Hz. The decrease of f_c is expected. In the Stokes flow regime, the rotational drag coefficient of a sphere at a distance h from a no-slip wall is higher than that in a bulk fluid. For h/r=1.5, this drag coefficient can be approximated very well using $\gamma = 8\pi\mu r^3\left(1+\frac{5}{16}\left(\frac{r}{h}\right)^3\right)$,[50] which predicts a drag coefficient that is 9.3% higher than that in bulk. Using this drag coefficient, Eq. 26 predicts an f_c of 18.3 Hz, in excellent agreement with our simulations. If the f_c determined in our simulations is used in Eq. 27, the variation of the sphere's mean rotational frequency

at $f_B > f_c$ is predicted accurately (see Fig. 6a). The rotational Reynolds number at f_c is $Re_{\omega,c}$=0.29 (the maximal Re_ω investigated in Fig. 6a is also around 0.29 since the sphere rotates slower than f_c once f_B exceeds f_c). These results suggest that, although Eq. 27 was derived for particles in unbounded fluids and with vanishing Re_ω, for Re_ω up to ~1, it can be used to predict the rotation of wall-confined particles if an accurate f_c is used. This is in line with the findings that the hydrodynamic torque experienced by a rotating sphere above a wall at $Re_\omega = 1$ is predicted well by solving the Stokes flow.[39]

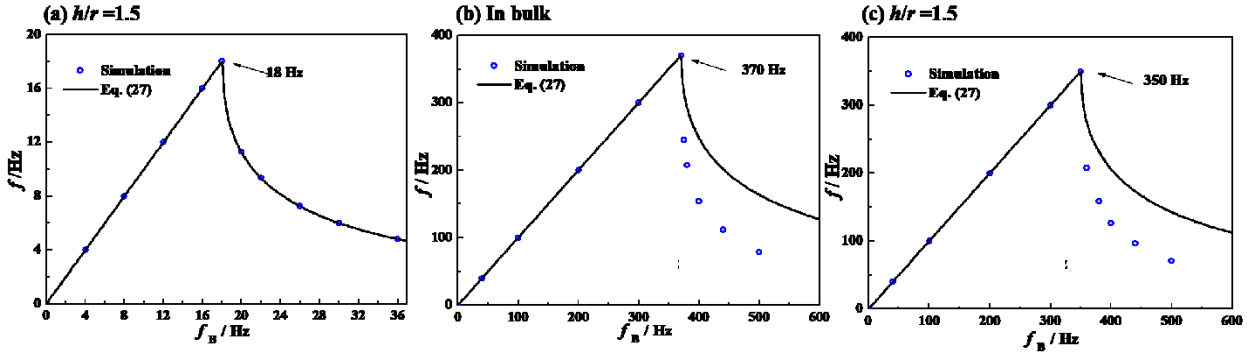

Figure 6. The mean frequency of a sphere actuated by a rotating magnetic field. (**a,c**) The sphere is positioned at $h = 1.5r$ above the lower wall and L=30r. (**b**) The sphere is in a bulk fluid. r = 48 μm and in all three cases. In (**a**), $M = 80\pi$ A/m; In (**b-c**), $M = 1600\pi$ A/m.

Next, we examine the effects of inertia on sphere's rotation at $Re_\omega > 1$. We simulate the rotation of a sphere (r = 48 μm; $M = 1600\pi$ A/m) in magnetic fields with f_B = 0 to 500 Hz. A naïve application of Eq. 26 predicts an f_c of 400 Hz, and the corresponding Re_ω is 5.79. Figures 6b and 6c show the mean rotational frequency of the sphere in bulk and at a distance $h = 1.5r$ above the lower wall, respectively. When immersed in bulk, the particle is seen to follow the rotating field up to 370 Hz; when positioned near a no-slip wall, the particle can follow the rotating field only up 350 Hz. Furthermore, in the asynchronous regime, the sphere's rotational frequency f decreases more rapidly with increasing f_B than that predicted by Eq. 27, even when the f_c computed in the simulations is used. When inertia plays an essential role in the fluids around the sphere, the hydrodynamic torque exerted by the fluids increases nonlinearly and faster with f than that predicted by the Stokes flow-based theories. Therefore, it is harder for the sphere to catch up with the rotating magnetic field in this flow regime, and consequently f_c and the sphere's mean rotational frequency in the asynchronous regime are smaller than the predictions by Eq. 26 and 27.

We now study how the translation of a magnetically actuated sphere is affected by inertia effects. To this end, the radius of the sphere is varied systematically while their magnetization M is kept to be the same as in Fig. 2. The frequency of the rotating magnetic field is f_B = 20 or 200 Hz, with which the sphere rotates with the applied field synchronously. Figure 7a shows that, for f_B = 20 Hz, the translation speed V_x increases linearly with the particle size. For f_B = 200 Hz, the increase of V_x becomes sublinear at r = 48 μm, and even decreases for spheres with radius larger than 72 μm.

Because nonlinearity becomes important at $\mathrm{Re}_\omega \gtrsim 1$ in Fig. 7a, the results in this figure are cast into the dimensionless form of $\mathrm{Re}_T = 2\rho V_x r/\mu$ as a function of Re_ω ($\mathrm{Re}_\omega = \rho\omega r^2/\mu$, see Fig. 7b). At $\mathrm{Re}_\omega \lesssim 1$, the data for f_B = 20 or 200 Hz collapse together with $\mathrm{Re}_T = 0.025\mathrm{Re}_\omega$. To understand this result, we note that the translation speed of a rotating sphere is determined by the balance between the rotation-induced driving force F_h (see Eq. 28) and the hydrodynamic drag experienced by a moving sphere F_d (see Eq. 31). Balancing F_h and F_d, we have

$$\frac{\mathrm{Re}_T}{\mathrm{Re}_\omega} = \frac{2V_x}{r\omega} = \frac{2}{r\omega}\frac{F_h}{6\pi\mu r f_u(h/r,\mathrm{Re}_T)} = \frac{f_x(h/r,\mathrm{Re}_\omega)}{3f_u(h/r,\mathrm{Re}_T)} \tag{34}$$

When $\mathrm{Re}_\omega \ll 1$ and $\mathrm{Re}_T \ll 1$, f_x and f_u are independent of Re_ω and Re_T, and are function of h/r only (see Eq. 30 and 32). For the h/r=1.5 used in our study, f_u = 1.616 and f_x = 0.117, respectively (see Fig. 2b and Table. 1). Hence $\mathrm{Re}_T/\mathrm{Re}_\omega = 0.024$, in agreement with the slope seen in Fig. 7b.

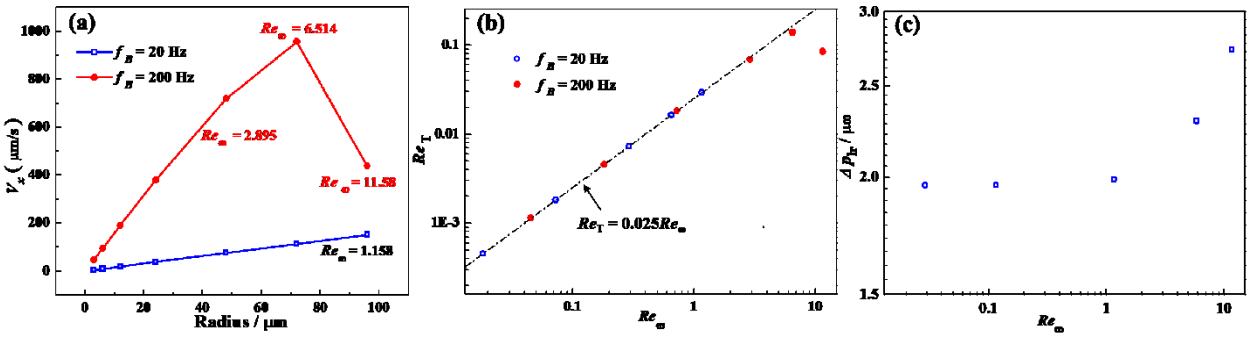

Figure 7. Effects of inertia on the translation of magnetic sphere actuated by a rotating magnetic field. (**a**) Variation of the sphere's translation velocity as a function of its radius under the action of magnetic fields with f_B= 20 and 200 Hz. (**b**) The data in (**a**) presented in the form of the sphere's translational *Re* number vs. rotational *Re* number. (**c**) Evolution of the difference between the maximal pressure in the bottom front side and the minimal pressure in the bottom back side of the sphere with the rotational Reynolds number.

As Re_ω increases beyond ~1.0, Re_T grows in a sublinear manner and eventually decreases. This is caused by the inertia-induced reduction of the hydrodynamic force propelling a rotating sphere laterally. Specifically, we perform separate simulations to measure the hydrodynamic force experienced by spheres rotating near a no-slip wall. At h/r = 1.5, f_x decreases from 0.117 to 0.096 and 0.032 as Re_ω increases from nearly zero to 6.514 and 11.58, respectively. The decrease f_x can be understood as follows.

When a sphere rotates near a semi-infinite wall in the clockwise direction, a net force F_x in the x-direction is developed on the sphere. The viscous component, $F_{vis,x}$, is in the x-direction. The pressure force, $F_{p,x}$, is in the negative x-direction because of the pressure difference at the bottom back and bottom front sides of the sphere (see Fig. 5a). To gauge the evolution of this pressure difference with Re_ω, we define a ΔP_{lr} as the difference between the maximal pressure in the bottom front region and the minimal pressure in the bottom back region of the sphere. Figure 7c shows that for $Re_\omega \ll 1$, $\Delta P_{lr}/\mu\omega$ is nearly a constant, consistent with the fact that, when inertia is weak, the pressure in the fluids has a characteristic value of $\mu V/r$ or $\mu\omega$ (as the characteristic velocity V is ωr here). As Re_ω increases beyond ~1.0, Fig. 7c shows that $\Delta P_{lr}/\mu\omega$ increases rapidly with Re_ω. This is because, as inertia becomes stronger, the Bernoulli effect emerges and ΔP_{lr} will increase faster than $\mu\omega$ (eventually, $\Delta P_{lr}/\mu\omega$ should scale as $\rho(r\omega)^2/\mu\omega$, although this is not observed under the modest Re_ω numbers used here). The deviation of $\Delta P_{lr}/\mu\omega$ from a constant and its rapid rise with Re_ω causes the pressure force acting on the sphere to become stronger, and thus f_x decreases, which in turn leads to the decrease of Re_T shown in Fig. 7b.

Actuation of free magnetic spheres

Here, we relax the assumption that the forces on an actuated sphere are balanced *a priori* in the vertical direction and study the actuation of free magnetic spheres. We consider gravity and buoyancy as the external forces. The density of ferromagnetic materials is typically 5-9 times that of the water (ρ). However, by coating these materials using polymers, the resulting magnetic particles can have a density of ~2-9ρ.[51] When placed in water, these particles will settle toward the wall beneath the water. However, a

sphere rotating above a wall can experience a lift force, making it possible for the particle eventually to reach an equilibrium height while translating laterally.

Figure 8a shows the lift force experienced by a sphere rotating above a no-slip wall fixed at h/r= 1.5. As in above subsection, the simulations are performed in the system shown in Fig. 1a with the upper wall located at z/r = 30, i.e., the sphere is essentially above an isolated wall. The lift force scaled by $\pi\rho r^4\omega^2$ is practically independent of Re_ω for Re_ω ~ 1-5 and decreases at even higher Re_ω. The latter is consistent with the data reported earlier.[39] The fact that the lift force scales linearly with $\rho r^4\omega^2$ is consistent with the fact that, even in the limit of small Re_ω, inertia associated with particle rotation cannot be neglected as far as the lift force is concerned. [38-39, 50, 52]

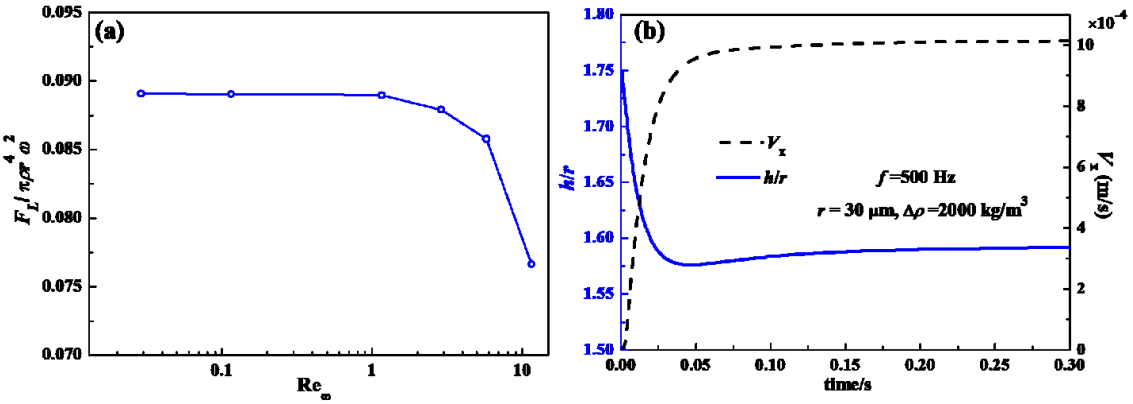

Figure 8. (**a**) The lift force experienced by a center-fixed sphere rotating above a no-slip wall. (**b**) Trajectory and instantaneous translation velocity of a sphere released from a height of h/r = 1.75 above a no-slip wall.

Next, we simulate the actuation of a free magnetic sphere. The sphere has a radius of 30 μm and a density of 3ρ. It is fixed at h/r = 1.75 initially. At t = 0, it is released and rotates synchronously with an applied magnetic field with a frequency of f = 500 Hz. Figure 8b shows the z-position and the instantaneous translation speed of the sphere as a function of time. The sphere first settles toward its equilibrium height, overshoots the equilibrium height slightly by $t \sim 20/f$, and comes to its equilibrium height at $h/r \approx 1.59$ by $t \sim 150/f$. The overshooting is caused by the fact that, when the sphere first approaches h/r = 1.59, its translational speed and the flow around it have not reached their steady state yet, which renders the instantaneous lift force smaller than that when the sphere is translating and rotating at the steady state.

Indeed, although the translational Reynolds number is small (<0.03), the circulating flow near the sphere takes time to reach its steady state. For example, for a sphere whose center is constrained at $h/r = 1.5$ but allowed to translate laterally, once it starts to rotate, its translational speed only reaches 90% of the steady value after about 42 r^2/ν (see Fig. S2 in the Supporting Information), which corresponds to $20/f$.

Overall, the above results indicate that, because of the lift force induced by the rotation of spheres, they may overcome gravity to reach an equilibrium height and move laterally. Therefore, results in first two subsections are useful for understanding the dynamics of free spheres actuated by external magnetic fields at the steady state. If the transient dynamics of a sphere (e.g., how it settles or lifts toward the equilibrium height) is of interest, then the unsteady NS equations generally have to be solved.

Conclusions

In this work, the immersed-boundary lattice Boltzmann method is adopted to simulate the magnetic actuation of spherical surface walkers confined between walls. By solving the full Navier-Stokes equations, our simulations are not limited to the Stokes regime, which allows us to examine the particle dynamics in presence of inertia and lift forces. We focus on how the surface walkers' translation motion is affected by type of confining boundaries, the degree of confinement, and the finite inertia of the fluids.

Our simulations show that both the nature of confining boundaries (slip *vs*. no-slip) and the degree of confinement significantly affect the dynamics of surface walkers. For example, for a sphere at a given height above a lower no-slip wall, while its translation speed often decreases as the upper wall is shifted toward it, its translational speed can increase dramatically if the upper wall features a slip surface (e.g., that of the air-water interface). On the other hand, if the upper wall features a no-slip surface, the sphere can reverse its translation direction when it becomes highly confined. Finite fluid inertia reduces the critical frequency of the rotating magnetic field, especially when the sphere is confined near a no-slip wall. Even when the sphere can rotate synchronously with the external magnetic field, its translation is hindered by inertia effects when the rotational Reynolds number becomes considerably larger than 1. When the rotational Reynolds number exceeds ~5, a sphere's translational Reynolds can even decrease with

increasing rotational Reynolds numbers. Because many applications of surface walkers involve confined geometries (e.g., when they are suspended in microchannels) and finite inertia (e.g., when the surface walkers are large or the frequency of the applied magnetic fields is high), the rich translation and rotation behaviors of surface walkers revealed here should be considered in their design and applications.

Supporting Information available: A nomenclature of all variables in this work, the distribution of fluid velocity near a rotating sphere, and evolution of the translation velocity of a sphere that is set to rotate impulsively.

Acknowledgment

R.Q. gratefully acknowledges the financial support of NSF under grant 1808307. This study is partially supported by the Key Project of International Joint Research of National Natural Science Foundation of China (51320105004) and a scholarship from the Chinese Scholarship Council to W.Z.F.

References

(1) Biswas, S.; Pomeau, Y.; Chaudhury, M. K., New Drop Fluidics Enabled by Magnetic-Field-Mediated Elastocapillary Transduction. *Langmuir* **2016**, 32 (27), 6860-6870.
(2) Zhang, R.; Kumar, N.; Ross, J. L.; Gardel, M. L.; de Pablo, J. J., Interplay of Structure, Elasticity, and Dynamics in Actin-Based Nematic Materials. *Proc. Natl. Acad. Sci. U.S.A.* **2018**, 115 (2), E124-E133.
(3) Elgeti, J.; Winkler, R. G.; Gompper, G., Physics of Microswimmers-Single Particle Motion and Collective Behavior: A Review. *Rep. Prog. Phys.* **2015**, 78 (5), 056601.
(4) Driscoll, M.; Delmotte, B., Leveraging Collective Effects in Externally Driven Colloidal Suspensions: Experiments and Simulations. *Curr. Opin. Colloid In.* **2019**, 40, 42-57.
(5) Yang, T.; Tasci, T. O.; Neeves, K. B.; Wu, N.; Marr, D. W., Magnetic Microlassos for Reversible Cargo Capture, Transport, and Release. *Langmuir* **2017**, 33 (23), 5932-5937.
(6) Yang, T.; Marr, D. W.; Wu, N., Superparamagnetic Colloidal Chains Prepared via Michael-Addition. *Colloid. Surface A.* **2018**, 540, 23-28.
(7) Fischer, P.; Ghosh, A., Magnetically Actuated Propulsion at Low Reynolds Numbers: Towards Nanoscale Control. *Nanoscale* **2011**, 3 (2), 557-563.
(8) Zhang, J.; Sobecki, C. A.; Zhang, Y.; Wang, C., Numerical Investigation of Dynamics of Elliptical Magnetic Microparticles in Shear Flows. *Microfluid Nanofluid* **2018**, 22 (8), 83.
(9) Cēbers, A.; Ozols, M., Dynamics of an Active Magnetic Particle in a Rotating Magnetic Field. *Phys. Rev. E* **2006**, 73 (2), 021505.
(10) Blake, J. In a Note on the Image System for a Stokeslet in a No-Slip Boundary, *Math. Proc. Cambridge*, Cambridge University Press: **1971**; pp 303-310.
(11) Martínez-Pedrero, F.; Tierno, P., Advances in Colloidal Manipulation and Transport via Hydrodynamic Interactions. *J. Colloid. Interf. Sci.* **2018**, 519, 296-311.
(12) Driscoll, M.; Delmotte, B.; Youssef, M.; Sacanna, S.; Donev, A.; Chaikin, P., Unstable Fronts and Motile Structures Formed by Microrollers. *Nat. Phys.* **2017**, 13 (4), 375-379.

(13) Sing, C. E.; Schmid, L.; Schneider, M. F.; Franke, T.; Alexander-Katz, A., Controlled Surface-induced Flows from the Motion of Self-assembled Colloidal Walkers. *Proc. Natl. Acad. Sci. U.S.A.* **2010**, 107 (2), 535-540.
(14) Tottori, S.; Zhang, L.; Qiu, F.; Krawczyk, K. K.; Franco-ObregцЁn, A.; Nelson, B. J., Magnetic Helical Micromachines: Fabrication, Controlled Swimming, and Cargo Transport. *Adv. Mater.* **2012**, 24 (6), 811-816.
(15) Peyer, K. E.; Zhang, L.; Nelson, B. J., Bio-Inspired Magnetic Swimming Microrobots for Biomedical Applications. *Nanoscale* 2013, 5 (4), 1259-1272.
(16) Zhu, L.; Huang, W.; Yang, F.; Yin, L.; Liang, S.; Zhao, W.; Mao, L.; Yu, X.; Qiao, R.; Zhao, Y., Manipulation of Single Cells Using a Ferromagnetic Nanorod Cluster Actuated by Weak AC Magnetic Fields. *Adv. Biosyst.* **2019**, 3 (1), 1800246.
(17) Tierno, P.; Golestanian, R.; Pagonabarraga, I.; Sagués, F., Controlled Swimming in Confined Fluids of Magnetically Actuated Colloidal Rotors. *Phys. Rev. Lett.* **2008**, 101 (21), 218304.
(18) Delmotte, B.; Driscoll, M.; Chaikin, P.; Donev, A., Hydrodynamic Shocks in Microroller Suspensions. *Phys. Rev. Fluids* **2017**, 2 (9), 092301.
(19) Martinez-Pedrero, F.; Ortiz-Ambriz, A.; Pagonabarraga, I.; Tierno, P., Colloidal Microworms Propelling via a Cooperative Hydrodynamic Conveyor Belt. *Phys. Rev. Lett.* **2015**, 115 (13), 138301.
(20) Martinez-Pedrero, F.; Navarro-Argemí E.; Ortiz-Ambriz, A.; Pagonabarraga, I.; Tierno, P., Emergent Hydrodynamic Bound States between Magnetically Powered Micropropellers. *Sci. Adv*. **2018**, 4 (1), eaap9379.
(21) Kaiser, A.; Snezhko, A.; Aranson, I. S., Flocking ferromagnetic colloids. *Sci. Adv.* **2017**, 3 (2), e1601469.
(22) Mahoney, A. W.; Nelson, N. D.; Peyer, K. E.; Nelson, B. J.; Abbott, J. J., Behavior of Rotating Magnetic Microrobots above the Step-out Frequency with Application to Control of Multi-Microrobot Systems. *Appl. Phys. Lett.* **2014**, 104 (14), 144101.
(23) Hackborn, W., Asymmetric Stokes Flow Between Parallel Planes Due to a Rotlet. *J. Fluid Mech.* **1990**, 218, 531-546.
(24) Bhattacharya, S.; Bławzdziewicz, J., Image System for Stokes-Flow Singularity Between Two Parallel Planar Walls. *J. Math. Phys.* **2002**, 43 (11), 5720-5731.
(25) Bhattacharya, S.; Bławzdziewicz, J.; Wajnryb, E., Hydrodynamic Interactions of Spherical Particles in Suspensions Confined Between Two Planar Walls. *J. Fluid Mech.* **2005**, 541, 263-292.
(26) Spagnolie, S. E.; Lauga, E., Hydrodynamics of Self-Propulsion Near a Boundary: Predictions and Accuracy of Far-field Approximations. *J. Fluid Mech.* **2012**, 700, 105-147.
(27) Swan, J. W.; Brady, J. F.; Moore, R. S.; 174, C., Modeling Hydrodynamic Self-Propulsion with Stokesian Dynamics. Or Teaching Stokesian Dynamics to Swim. *Phys. Fluids* **2011**, 23 (7), 071901.
(28) Krishnamurthy, S.; Yadav, A.; Phelan, P.; Calhoun, R.; Vuppu, A.; Garcia, A.; Hayes, M., Dynamics of Rotating Paramagnetic Particle Chains Simulated by Particle Dynamics, Stokesian Dynamics and Lattice Boltzmann Methods. *Microfluid Nanofluid* **2008**, 5 (1), 33-41.
(29) Gao, Y.; Hulsen, M.; Kang, T.; Den Toonder, J., Numerical and Experimental Study of a Rotating Magnetic Particle Chain in a Viscous Fluid. *Phys. Rev. E* **2012**, 86 (4), 041503.
(30) Yeo, K.; Lushi, E.; Vlahovska, P. M., Collective Dynamics in a Binary Mixture of Hydrodynamically Coupled Microrotors. *Phys. Rev. Lett.* **2015**, 114 (18), 188301.
(31) Climent, E.; Yeo, K.; Maxey, M. R.; Karniadakis, G. E., Dynamic Self-assembly of Spinning Particles. *J. Fluid Eng.* **2007**, 129 (4), 379-387.
(32) Ali, J.; Kim, H.; Cheang, U. K.; Kim, M. J., Micro-PIV Measurements of Flows Induced by Rotating Microparticles Near a Boundary. *Microfluid Nanofluid* **2016**, 20 (9), 131.
(33) Khaderi, S.; den Toonder, J.; Onck, P., Microfluidic Propulsion by the Metachronal Beating of Magnetic Artificial Cilia: A Numerical Analysis. *J. Fluid Mech.* **2011**, 688, 44-65.
(34) Zhang, R.; Roberts, T.; Aranson, I. S.; De Pablo, J. J., Lattice Boltzmann Simulation of Asymmetric Flow in Nematic Liquid Crystals with Finite Anchoring. *J. Chem. Phys.* **2016**, 144 (8), 084905.
(35) de Graaf, J.; Menke, H.; Mathijssen, A. J.; Fabritius, M.; Holm, C.; Shendruk, T. N., Lattice-Boltzmann Hydrodynamics of Anisotropic Active Matter. *J. Chem. Phys.* **2016**, 144 (13), 134106.
(36) Khaderi, S.; Baltussen, M.; Anderson, P.; Den Toonder, J.; Onck, P., Breaking of Symmetry in Microfluidic Propulsion Driven by Artificial Cilia. *Phys. Rev. E* **2010**, 82 (2), 027302.
(37) Baltussen, M.; Anderson, P.; Bos, F.; den Toonder, J., Inertial Flow Effects in a Micro-Mixer Based on Artificial Cilia. *Lab Chip* **2009**, 9 (16), 2326-2331.

(38) Zeng, L.; Balachandar, S.; Fischer, P., Wall-induced Forces on a Rigid Sphere at Finite Reynolds Number. *J. Fluid Mech.* **2005**, 536, 1-25.
(39) Liu, Q.; Prosperetti, A., Wall Effects on a Rotating Sphere. *J. Fluid Mech.* **2010**, 657, 1-21.
(40) Wu, J.; Shu, C., Implicit Velocity Correction-based Immersed Boundary-Lattice Boltzmann Method and Its Applications. *J. Comput. Phys.* **2009**, 228 (6), 1963-1979.
(41) Tian, F.B.; Luo, H.; Zhu, L.; Liao, J. C.; Lu, X.Y., An Efficient Immersed Boundary-Lattice Boltzmann Method for the Hydrodynamic Interaction of Elastic Filaments. *J. Comput. Phys.* **2011**, 230 (19), 7266-7283.
(42) Suzuki, K.; Inamuro, T., Effect of Internal Mass in the Simulation of a Moving Body by the Immersed Boundary Method. *Comput. Fluids* **2011**, 49 (1), 173-187.
(43) Feng, Z.G.; Michaelides, E. E., Robust Treatment of No-slip Boundary Condition and Velocity Updating for the Lattice-Boltzmann Simulation of Particulate Flows. *Comput. Fluids* **2009**, 38 (2), 370-381.
(44) Zhang, D.; Papadikis, K.; Gu, S., Three-Dimensional Multi-Relaxation Time Lattice-Boltzmann Model for the Drop Impact on a Dry Surface at Large Density Ratio. *Int. J. Multiphas. Flow* **2014**, 64, 11-18.
(45) Fang, W.Z.; Tang, Y.Q.; Yang, C.; Tao, W.Q., Numerical Simulations of the Liquid-Vapor Phase Change Dynamic Processes in a Flat Micro Heat Pipe. *Int. J. Heat Mass Tran.* **2020**, 147, 119022.
(46) Kang, S. K.; Hassan, Y. A., A Comparative Study of Direct-Forcing Immersed Boundary-Lattice Boltzmann Methods for Stationary Complex Boundaries. *Int. J. Nume.r Meth. Fl.* **2011**, 66 (9), 1132-1158.
(47) Krüger, T.; Kusumaatmaja, H.; Kuzmin, A.; Shardt, O.; Silva, G.; Viggen, E. M., The Lattice Boltzmann Method. Springer International Publishing **2017**, 10, 978-3.
(48) Jorge, G. A.; Llera, M. a.; Bekeris, V., Magnetic Particles Guided by Ellipsoidal AC Magnetic Fields in a Shallow Viscous Fluid: Controlling Trajectories and Chain Lengths. *J. Magn. Magn. Mater.* **2017**, 444, 467-471.
(49) Romodina, M. N.; Lyubin, E. V.; Fedyanin, A. A., Detection of Brownian Torque in a Magnetically-Driven Rotating Microsystem. *Sci. Rep*. **2016**, 6, 21212.
(50) Goldman, A. J.; Cox, R. G.; Brenner, H., Slow Viscous Motion of a Sphere Parallel to a Plane Wall-I Motion Through a Quiescent Fluid. *Chem. Eng. Sci.* **1967**, 22 (4), 637-651.
(51) Philippova, O.; Barabanova, A.; Molchanov, V.; Khokhlov, A., Magnetic Polymer Beads: Recent Trends and Developments in Synthetic Design and Applications. *Eur. Polym. J.* **2011**, 47 (4), 542-559.
(52) Rubinow, S.; Keller, J. B., The Transverse Force on a Spinning Sphere Moving in a Viscous Fluid. *J. Fluid Mech.* **1961**, 11 (3), 447-459.